RESEARCH ARTICLE

ADVANCED
MATERIALS
INTERFACES
Open Access

www.advmatinterfaces.de

Plasma-Enhanced Magnetron Sputtering: A Novel Approach for Biofunctional Metal Nanoparticle Coatings on Reverse Osmosis Composite Membranes

Nicole Michler,* Ulrike M. Hirsch, Carolin Steinert, Gregor Fritzsche, and Christian E. H. Schmelzer

Reverse osmosis (RO) is the most common method for treating salt and brackish water. As a membrane-driven process, a key challenge for RO systems is their susceptibility to scaling and biofouling. To address these issues, functional coatings utilizing metal nanoparticles (MNPs) are developed. In this study, silver, gold, and copper nanoparticles are applied onto thin-film composite (TFC) membranes using plasma-enhanced magnetron sputtering. The elemental composition, surface morphology, and hydrophilicity of the coatings are analyzed using X-ray photoelectron spectroscopy (XPS), scanning electron microscopy (SEM), and contact angle measurements. The antimicrobial properties and the filtration efficiency of the coated membranes are assessed through application-specific experimental setups. Silver and copper nanoparticles exhibit superior antimicrobial properties, reducing microorganism adhesion by a factor of 10^3 compared to uncoated membranes. Under appropriate coating conditions, no deterioration in filtration performance is observed. Enhancing the adhesion of MNPs is necessary for achieving sustained release of metal ions.

1. Introduction

To address the global challenges of water scarcity and surface water contamination, it is essential to tap new water resources and advance water treatment technologies.[1] Over the past decades, membrane-driven separation processes have largely replaced thermal desalination methods. Currently, RO is recognized as the standard method for the desalination of saline and brackish water, comprising 69% of the global desalination capacity.[2]

Conventional TFC membranes used in RO systems feature a multilayer structure consisting of a highly crosslinked aromatic polyamide (PA) layer, a porous polysulfone (PSU) support layer, and a polyethylene terephthalate (PET) substrate. The PA layer, typically less than 100 nm thick, serves as the active separating layer. It is characterized by a dense, nonporous structure and high mechanical resistance. RO systems, known for their energy efficiency, superior filtration performance, and scalability, offer distinct advantages over other desalination methods such as multi-effect distillation (MED) and multi-stage flash distillation (MSF). In the past few years, significant progress has been made in enhancing the energy efficiency of membrane-based desalination processes and in developing innovative strategies for brine management.[3–8]

Despite these technological advancements, biofouling continues to impose significant economic challenges on the operation of RO-based desalination plants. Biofilm formation adversely affects the active separating layer of RO membranes, leading to flux decline, increased energy consumption, diminished permeate quality, and higher maintenance costs.[9] Developing sustainable antifouling strategies is essential to boost the operational performance and environmental sustainability of RO.

To date, numerous strategies have been developed to mitigate biofouling.[10,11] Among the material-based strategies, modifying the membrane surface with anti-adhesive or biocidal coatings has emerged as a particularly promising method for reducing biofouling.[12–18]

MNPs are recognized for their excellent antimicrobial properties, which are based on non-specific, multifaceted mechanisms.[19] These include the impairment of the respiratory chain, the release of reactive oxygen species, and the interaction with biomolecules.[20–22] MNPs exhibit a broad spectrum of antimicrobial activity that effectively prevents the development of resistance.[19] Various techniques have been used to deposit MNPs on RO membranes, such as

N. Michler, U. M. Hirsch, C. Steinert, G. Fritzsche, C. E. H. Schmelzer
Department of Biological and Macromolecular Materials
Fraunhofer Institute for Microstructure of Materials and Systems IMWS
Walter-Hülse-Str. 1, 06120 Halle (Saale), Germany
E-mail: nicole.michler@imws.fraunhofer.de
N. Michler, C. Steinert, G. Fritzsche, C. E. H. Schmelzer
Martin Luther University Halle-Wittenberg
Universitätsplatz 10, 06108 Halle (Saale), Germany

**ADVANCED
SCIENCE NEWS**

www.advancedsciencenews.com

**ADVANCED
MATERIALS
INTERFACES**
Open Access

www.advmatinterfaces.de
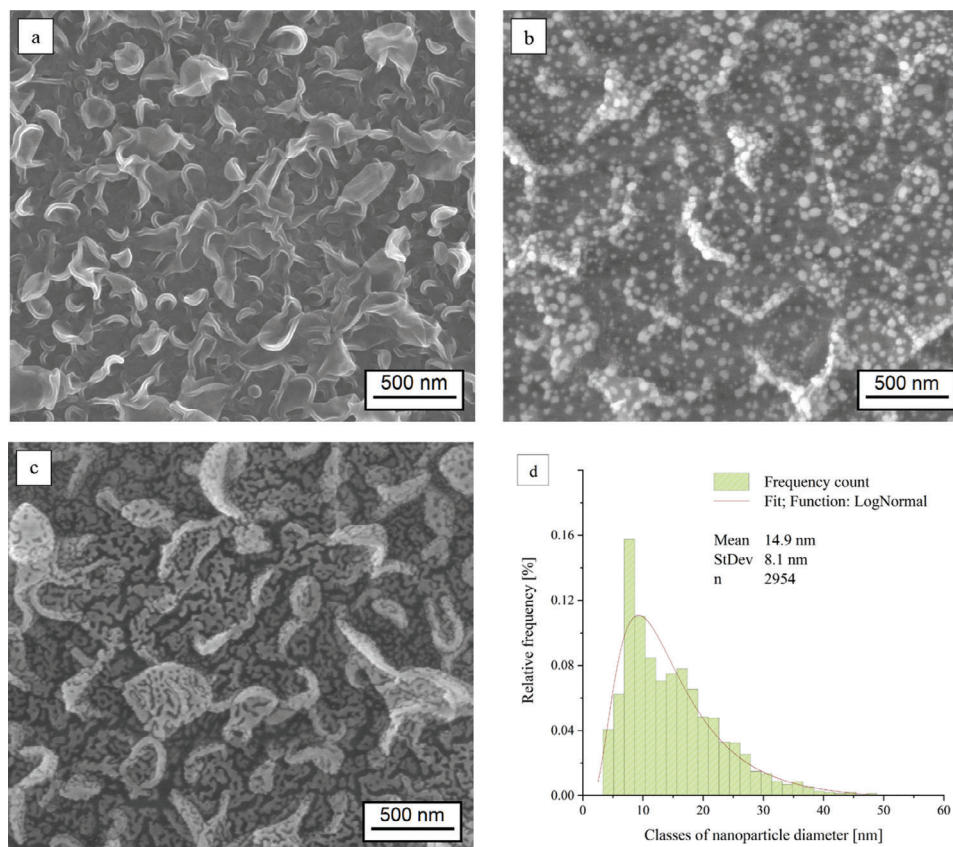
Figure 1. Surface morphology of native and MNP-coated RO membranes. SEM micrographs of a) uncoated, b) silver-coated, and c) gold-coated RO membrane surfaces, d) histogram of silver nanoparticle diameters.

chemical reduction, thiol coupling, green synthesis, impregnation via interfacial polymerization, and arc plasma deposition.[23–28] In a previous study conducted by our group, it was shown that plasma-assisted magnetron sputtering is a suitable technique for the controlled deposition of silver nanoparticles.[29]

Vacuum-based coating processes, such as plasma-assisted magnetron sputtering, offer major advantages over conventional wet-chemical coating techniques in terms of deposition rate, coating uniformity, and controllability of the deposition process. A wide range of materials, including metals, alloys, oxides, and even polymers, can be applied, providing the flexibility needed for developing customized coatings for specific applications. On an industrial scale, the functionalization of RO membranes can be implemented as a continuous roll-to-roll process, ensuring high throughput.

In the present study, the suitability of plasma-assisted magnetron sputtering for the deposition of metallic thin films on RO membranes was further evaluated. Three different MNP species- gold (Au), copper (Cu), and silver (Ag)- were investigated with respect to their layer structure, antimicrobial properties, and coating stability. These metals were selected due to their well-documented antimicrobial effect and their distinct physicochemical properties.[30–32] A comparative assessment regarding their biofunctional performance is presented.

2. Results and Discussion

2.1. Morphology

Figures 1a–c illustrate SEM micrographs of uncoated, gold-coated, and silver-coated RO membrane surfaces. The polyamide layer of the native membrane surface exhibits a typical ridge-and-valley structure, as previously described in detail.[33,34] This structure forms at the interface between the polar and non-polar phases during the interfacial polymerization step of the manufacturing process. Surface roughness parameters of the native membrane can be found in the supporting information (see Figure S1, Supporting Information).

With a total coating time of 15 s, silver forms discrete, nearly round-shaped particles with an average diameter of 14.9 nm $\pm$ 8.1 nm (Figure 1b). The particle size distribution of silver is shown in Figure 1d.

Under similar coating conditions, gold forms nanostructures arranged in a much more cohesive manner, though not forming a completely closed layer, resembling a nanostructure near the percolation transition (see Figure 1c).

Since no wetting layer forms on the substrate surface, it can be assumed that the growth of the metal nanoparticles follows a Volmer-Weber mechanism.[35] This growth mechanism is characterized by island-like nanostructures with a high specific surface area.
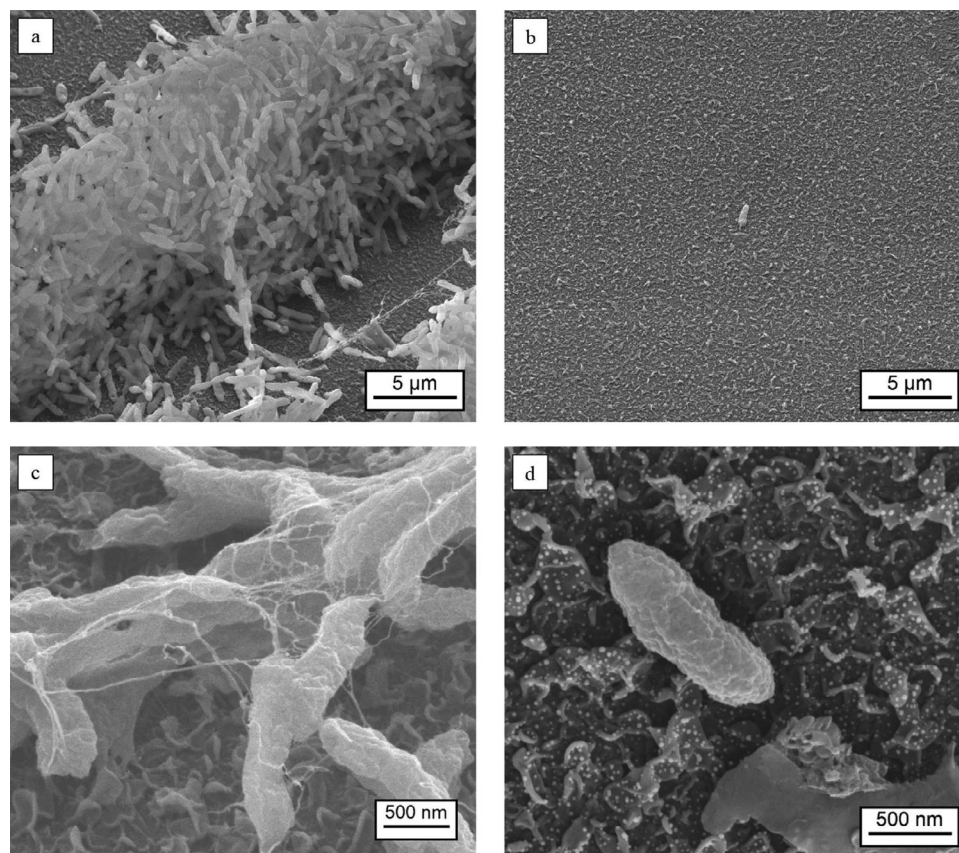
2400461 (2 of 10)
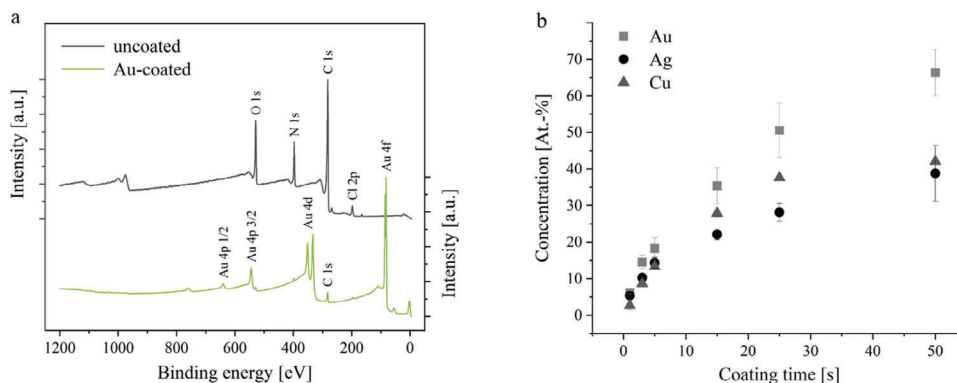
Figure 2. Elemental composition of MNP-coated RO membranes. a) XPS survey spectra of a native and a gold-coated TFC membrane ($t = 3 \times 5$ s, $P = 200$ W), b) Elemental composition measured as a function of total coating time.

The morphologically determined degree of coverage is 39% for gold and 28% for silver. Unlike silver and gold, discrete nanostructures were not observed for copper (see Figure S2, Supporting Information). This absence may be due to the nanoparticle diameter being below the resolution limit of the SEM. However, energy-dyipersive X-ray spectroscopy (EDS) mappings of the copper-coated membrane indicate a homogeneous metal distribution with an average mass fraction of 3.4% ± 0.3%.

After deposition, the metal nanoparticles undergo complex rearrangement and reaction processes, which are accompanied by macroscopically visible color changes.[35,36] For silver-coated membranes, an immediate color change from violet to yellow is observed. Gold coatings exhibit a slow color transition from light gray to brownish violet, while copper coatings show no pronounced color change and maintain a pale green coloration.
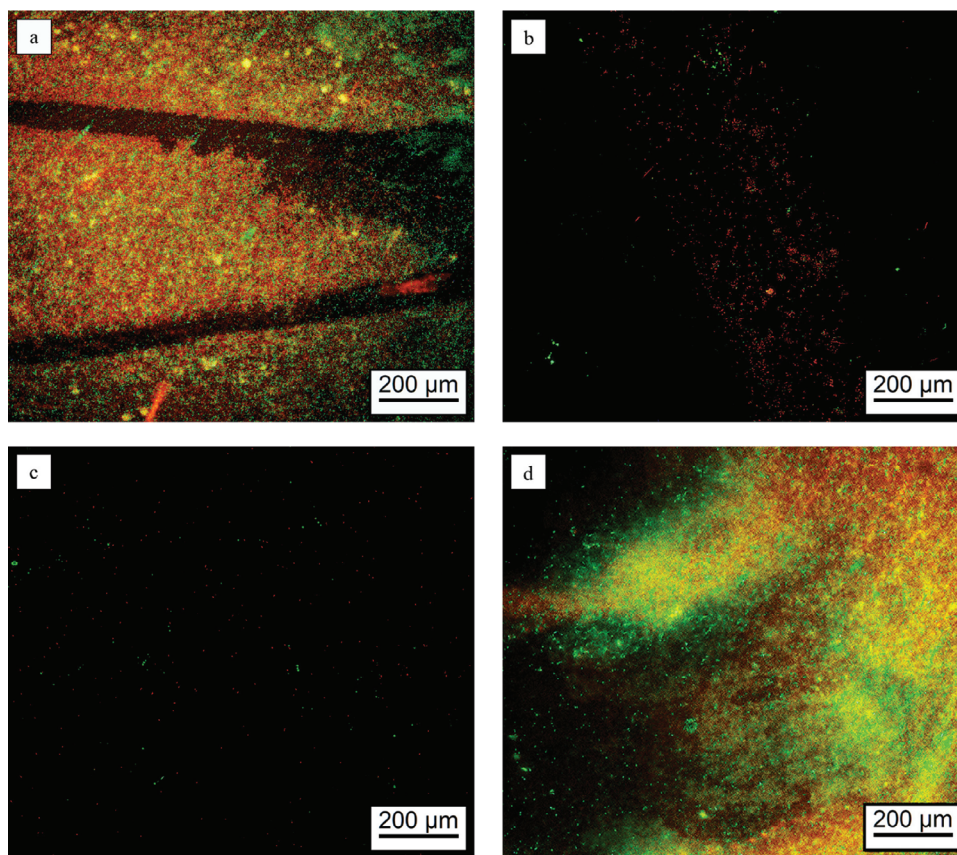
Figure 3. Fluorescence micrographs of *P. protegens* on native and MNP-coated RO membranes after Syto 9 and propidium iodide staining. Viable bacteria appear green, and non-viable bacteria appear red. Coating: a) Au, 3×5 s, 200 W; b) Ag, 3×5 s, 200 W; c) Cu, 3×5 s, 200 W, d) native RO membrane.

2400461 (3 of 10)

**ADVANCED
SCIENCE NEWS**

www.advancedsciencenews.com

**ADVANCED
MATERIALS
INTERFACES**
Open Access

www.advmatinterfaces.de

Figure 4. SEM micrographs of *P. protegens* on native and MNP-coated RO membranes at different magnifications. Left side: Native membrane surface a,c); right side: Ag-coated RO membrane (*t* = 3 x 5 s, *P* = 200 W) b, d).

2.2. Elemental Composition

The metal concentration on the membrane surface was investigated by XPS as a function of coating time. The information depth of XPS is ≈10 nm, making it much more surface-sensitive than EDS analysis, which has an information depth of> 300 nm under the experimental conditions described previously. Due to this low information depth, the growth behavior of the nanoparticles (particle diameter and distribution) may influence the measurement results.

Figure 2a shows representative XPS spectra of an uncoated and a gold-coated TFC membrane. The composition of the native membrane surface is ≈73% carbon, 12% oxygen, and 11% nitrogen, consistent with the nominal structure of aromatic polyamide. The presence of chlorine on the native membrane surface is attributed to unreacted functional groups of trimesoyl chloride during the manufacturing process.

Gold exhibits characteristic peaks at binding energies of 759 eV (Au 4s), 644 eV (Au 4p 1/2), 546 eV (Au 4p 3/2), 352 eV (Au 4d 3/2), 334 eV (Au 4d 5/2), 87.7 eV (Au 4f 5/2), and 84 eV (Au 4f 7/2). As shown in Figure 2a, the highly effective cross-section of gold results in sharp peaks with correspondingly high intensity and area fraction, making minor membrane components barely visible. For quantification, the corresponding R.S.F. values (e.g., 6.25 for Au 4f) were used. With a total coating time of 15 s, the gold concentration on the membrane surface is 34.9% ± 6.1%.
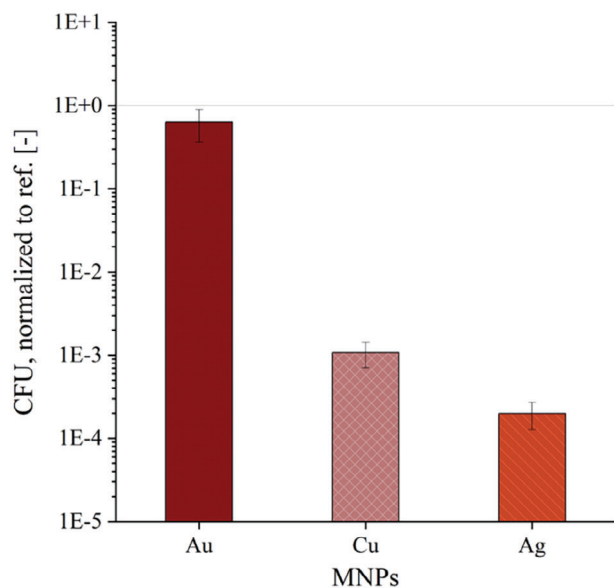
Using the same sputtering parameters, the copper and silver content on the membrane surface is significantly lower, amounting to 27.9% ± 1.0% and 21.3% ± 1.1%, respectively (see Figure S3, supporting information). It should be noted that high copper contents are always accompanied by high oxygen concentrations, far exceeding the oxygen content of the native membrane (see Figure 6). This indicates that copper nanoparticles immediately form a passivation layer of copper oxide.

For a given pressure, power, and target-substrate distance, the deposition rate largely depends on the material-specific sputter yield and the occurrence of scattering losses.[37] From the elemental analysis results, it can be deduced that the deposition rate is highest for gold, followed by copper and silver.

As shown in Figure 2b, with increasing coating time, the metal content on the membrane surface further increases, following a limited growth model with flattening curve progression. The formation of a continuous metal layer was not observed within the measurement range investigated.

2.3. Antimicrobial Performance

Figure 3 shows fluorescence micrographs of *Pseudomonas protegens* bacteria on native and MNP-coated membranes. To evaluate the proportions of viable and non-viable bacteria, differential staining was performed using Syto 9 (fluorescence

**ADVANCED
SCIENCE NEWS**

www.advancedsciencenews.com

**ADVANCED
MATERIALS
INTERFACES**
Open Access

www.advmatinterfaces.de

Figure 5. CFU count in the supernatant solutions of MNP-coated membranes, normalized to the reference (ref.; native membrane).

emission maximum at 503 nm, green) and propidium iodide (fluorescence emission maximum at 617 nm, red). Both staining agents serve as nuclear and chromosome counterstains. Syto 9 penetrates intact prokaryotic cell membranes, staining viable bacteria green, while propidium iodide accumulates in non-viable bacterial cells, staining them red.

As shown in Figure 3, dense microbial biofilms have formed on both the native (d) and gold-coated (a) membrane surfaces. The fluorescence micrographs were taken at the peripheral region of the samples to allow differentiation between the substrate and the biofilm. In the central areas, complete coverage with *P. protegens* can be observed. The biofilms contain roughly equal proportions of viable (green) and non-viable (red) bacteria.

Based on the fluorescence micrographs, no antimicrobial activity was observed for the gold coatings. In contrast, only single and predominantly non-viable bacteria are seen on the silver- and copper-coated membranes, indicating substantial antimicrobial activity.

Figure 4 shows SEM micrographs of *P. protegens* on native and silver-coated RO membranes at different magnifications. On the native membrane surface (a), densely packed, 3D bacterial growth structures are visible, indicative of the exponential growth phase of biofilm formation. The close-up (c) shows fibrous structures between the bacterial cells, forming the extracellular matrix of bacterial biofilms. However, extracellular polymeric substances (EPS) production is only weakly developed in the samples investigated. A study by Ueda and Saneoka suggested that *P. protegens* might tightly regulate EPS production.[38] They observed very limited EPS production by *P. protegens* under dynamic culture conditions, which aligns with the findings of this work.

Only single bacterial cells were found on silver-coated membranes (b), indicating that cell proliferation was quantitatively inhibited. The close-up (d) shows a bacterial cell surrounded by silver nanoparticles. Formless organic matter, likely lysed

bacterial cells, was found in several locations on the membrane surface (see Figure 4d, bottom right). SEM micrographs of *P. protegens* on gold- and copper-coated membranes can be found in the supporting information (see Figure S4, Supporting Information).

As a complementary method, the number of viable cells in the supernatant suspension was determined. **Figure 5** shows the number of colony-forming units (CFUs) as a function of coating type, with all values normalized to the reference value (uncoated membrane).

A logarithmic reduction factor of 3.7 ± 0.1 and 3.1 ± 0.2 was determined for silver- and copper-coated membranes, respectively (**Table 1**). This corresponds to a $> 99.8\%$ reduction in bacterial growth.

A reproducible, albeit weak, antimicrobial effect was also measured for gold-coated membranes, with bacterial growth in the supernatant solution reduced by an average of 25%. The statistical analysis found that the number of viable cells in the supernatant of gold-coated membranes was not significantly different from the reference (t-test with independent samples, $\alpha = 0.05$).

The antimicrobial effect of gold nanoparticles is controversially debated in the literature. Experimental results range from statistically significant biofilm inhibition to a very weak or absent antibacterial effect of bare gold nanoparticles.[39–42]

The comparatively weak antimicrobial effect is attributed to the stability and inertness of gold, which limits its bioavailability and reduces the probability of physiological interactions.[43] Previous studies have shown that the biofunctional activity of gold is dependent on particle size and surface chemistry.[44] In contrast to gold nanoparticles, gold nanoclusters and ionic complexes exhibit strong antimicrobial activity.[40,44] Moreover, it has been reported that Gram-positive bacteria show a stronger response to gold than Gram-negative ones.[45,46]

2.4. Filtration Performance

The filtration performance of native and MNP-coated RO membranes was evaluated by measuring their salt retention (**Figure 6a**) and permeability (Figure 6b) under application-oriented test conditions. As shown in Figure 6a, the salt retention of the MNP-coated membranes is $\approx 98.7\%$ of the reference value, with further increases observed with extended operating time, indicating that no permanent deterioration of the active separation layer occurred.

Drying RO membranes is inherently challenging; according to the manufacturer's recommendations, thin-film composite membranes must be stored wet after initial wetting to avoid irreversible loss in filtration performance. Membrane deterioration can be attributed to structural changes in the substrate, such as irreversible densification of the porous microstructure

Table 1. Logarithmic reduction factor of antimicrobial MNP coatings.

	Log_{10} $(\text{CFU}_0/\text{CFU})$ [-]
Au	0.2 ± 0.2
Cu	3.1 ± 0.2
Ag	3.7 ± 0.1
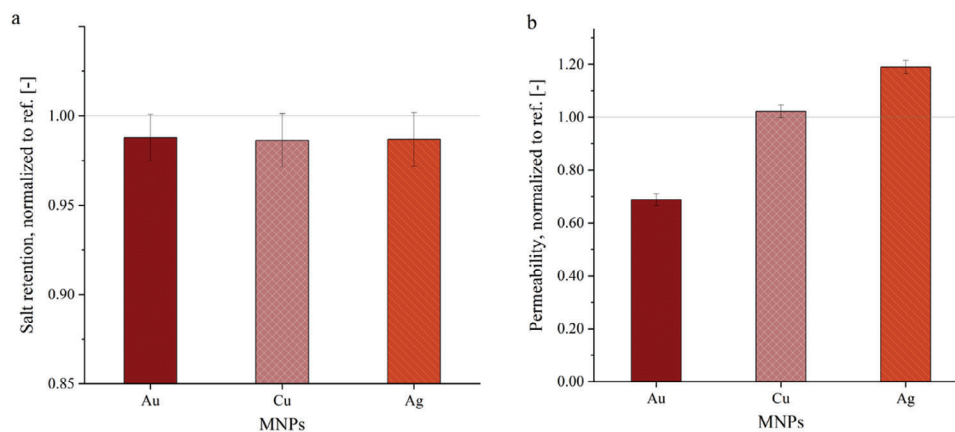
Figure 6. Salt retention a) and permeability b) of MNP-coated membranes, normalized to the reference (ref., native membrane); coating parameters: $P = 200$ W, $t = 3 \times 5$ s.

of the PSU ultrafiltration membrane, as well as changes in the polyamide layer.[33,47,48] In this study, complete regeneration of membrane performance was achieved through immersion treatment in phosphate-buffered saline solution (PBS) prior to drying. Organic and inorganic alkali metal salts improve the drying resistance of the PSU substrate as humectants; at the same time, ions can interact complexly with the active separation layer of the RO composite membrane, promoting the dissociation of the polymer network.[49,50] Further mechanistic investigations are required to elucidate the effects of the immersion treatment.

While it was demonstrated that performance-preserving vacuum coating is fundamentally possible, significant differences are evident between the coating types regarding permeability (Figure 6b). The gold-coated RO membrane exhibits considerably reduced permeability, attributed to clogging of the active separating layer. SEM micrographs (see Figure 1b) indicate that gold forms nanostructures near the percolation transition, resulting in a high degree of coverage. Increased sputter coating time progressively decreases membrane permeability, reducing it to 43% of the reference value after a total coating time of 75 s.

No clogging effects were observed for silver- and copper-coated membranes; the permeability of silver-coated membranes was even higher than that of the reference membrane. This improved permeability is attributed to increased surface hydrophilicity. **Table 2** shows the results of contact angle measurements on MNP-coated and native membranes.

The native RO membrane possesses intrinsic hydrophilic surface properties. Contact angles of $35.9° \pm 3.0°$ with water and $17.8° \pm 3.3°$ with diiodomethane were measured. The surface energy of the native membrane was determined to be 70.3 mN

m⁻¹, consisting of a polar fraction of 21.9 mN m⁻¹ ± 1.5 mN m⁻¹ and a dispersive fraction of 48.4 mN m⁻¹ ± 0.9 mN m⁻¹. The hydrophilic properties of the surface are further increased by applying a MNP coating. Due to their high specific surface area, MNPs exhibit excellent hydrophilic properties.[51]
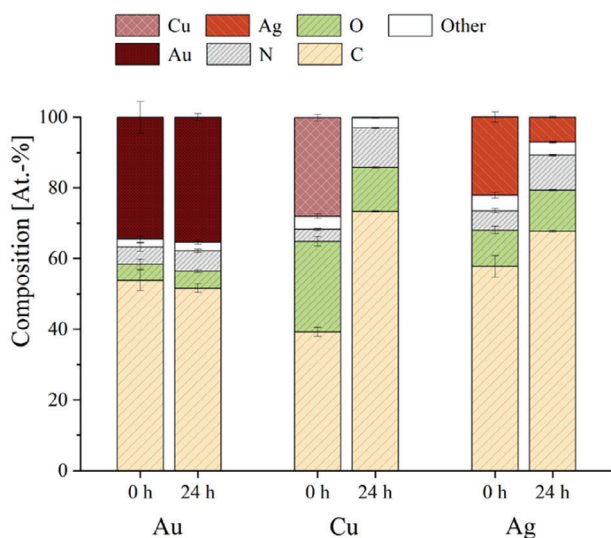
For copper, however, a time-dependent change in surface energy was observed. With increasing storage time (RT, air), the copper-coated membranes became more hydrophobic. Six days after coating application, a water contact angle of $63.2° \pm 4.1°$ was measured. This wettability transition to hydrophobic surface properties is well-known from copper metal foams and is usually attributed to the formation of an oxide passivation layer.[52] Partial oxidation of copper nanoparticles is confirmed by XPS data showing a notably high oxygen content on copper-coated membranes (see **Figure 7**). However, copper oxides are also known to improve the surface hydrophilicity of polymers.[53] Shirazy et al. propose that the transition from hydrophilic to hydrophobic surface properties is not a consequence of oxidation processes, but rather based on the adsorption of volatile organic components from ambient air.[52] A similar mechanism was previously described for superhydrophilic TiO_2 thin films.[54]

2.5. Coating Stability Testing

In aqueous media, MNP coatings are subject to dissolution processes that lead to coating degradation. Short-term elution tests were performed to determine the coating stability. Figure 7 shows the composition of MNP-coated membranes before and after elution with sodium chloride solution (2 g L⁻¹) and **Table 3** shows

Table 2. Contact angle and surface energy of native (ref.) and MNP-coated RO membranes.

	Contact angle θ_c [°] Diiodomethane	Contact angle θ_c [°] Water	Surf. energy σ_s [mN m⁻¹]	Surf. energy σ_p [mN m⁻¹] Polar	Surf. energy σ_d [mN m⁻¹] Dispersive
ref.	17.8 ± 3.3	35.9 ± 3.0	70.3 ± 2.4	21.9 ± 1.5	48.4 ± 0.9
Au	13.8 ± 2.9	23.9 ± 2.2	76.0 ± 1.5	49.3 ± 0.6	26.7 ± 0.9
Cu	12.9 ± 1.3	14.1 ± 2.1	79.1 ± 0.8	49.5 ± 0.3	29.6 ± 0.5
Ag	15.2 ± 2.4	20.9 ± 1.8	76.9 ± 1.2	49.0 ± 0.6	27.9 ± 0.7

**ADVANCED
SCIENCE NEWS**

www.advancedsciencenews.com

**ADVANCED
MATERIALS
INTERFACES**
Open Access

www.advmatinterfaces.de

Figure 7. Composition of MNP-coated RO membranes before and after elution testing (XPS).

the metal concentration in the corresponding eluate.

The gold concentration on the membrane surface remained largely stable under the selected experimental conditions, with only small amounts of gold dissolving into the solution. This stability was maintained even with longer elution times of up to 480 h. In contrast, the silver- and copper-coated membranes exhibited a significant decrease in metal concentration even after short test intervals. Elution for 24 h at a shaking speed of 80 rpm resulted in a silver loss of 67.9% and a copper loss of 99.2%. Correspondingly, the metal concentration in the eluate increased substantially.

In addition to dissolution processes, nanoparticle detachment may also contribute to coating disintegration. To gain a better understanding of the underlying mechanisms, the morphology of the silver-coated membranes was studied by SEM before and after elution. **Figure 8** shows a false-color illustration of the particle size distribution of silver nanoparticles on the membrane surface before and after 24 h of elution in aqueous sodium chloride solution (2 g L^{-1}).

It was found that the mean particle diameter increased significantly from 14.9 nm ± 8.1 nm to 29.1 nm ± 14.6 nm upon immersion in sodium chloride solution, as did the mean distance between the nanoparticles (t-test with paired samples, $\alpha = 0.05$). This suggests that a combination of dissolution, detachment, and rearrangement processes, such as coalescence and Ostwald ripening, contributes to the observed changes in particle size distribution and chemical composition.

Table 3. Metal concentration in the eluate determined by inductively coupled plasma mass spectrometry (ICP-MS).

	Concentration [µg L^{-1}]
Au	0.20 ± 0.06
Cu	61.27 ± 3.36
Ag	19.59 ± 0.96

To achieve a long-lasting antimicrobial effect, the coating stability needs to be improved. Previous studies have demonstrated that the adhesion of sputtered metal nanoparticle thin films depends on the surface energy of the substrate polymer and the sputtering parameters used.[55] Preconditioning of the RO membrane surface, such as through plasma activation or functionalization with thiol groups, might enhance coating adhesion and prevent MNP detachment. The chemical stability of the metals and their particle size are key factors in determining their dissolution properties. The dissolution of MNPs can be quantitatively inhibited by passivation.[56] Various capping agents, including cysteine, polyvinylpyrrolidone, tri-sodium citrate, and chitosan, have been successfully used for this purpose.[56–58] It is crucial to develop a passivation strategy for sputtered MNP thin films post-deposition while maintaining both filtration performance and antimicrobial activity.

3. Conclusion

Sputtered silver and copper nanoparticle coatings exhibit superior antimicrobial activity, effectively reducing bacterial growth on membrane surfaces by up to 99.8% in static suspension tests. In contrast, gold nanoparticle coatings demonstrated limited antimicrobial efficacy due to the metal's low solubility and weak oligodynamic effect. To sustain antimicrobial performance, enhancing the adhesion and chemical stability of silver and copper nanoparticles is crucial.
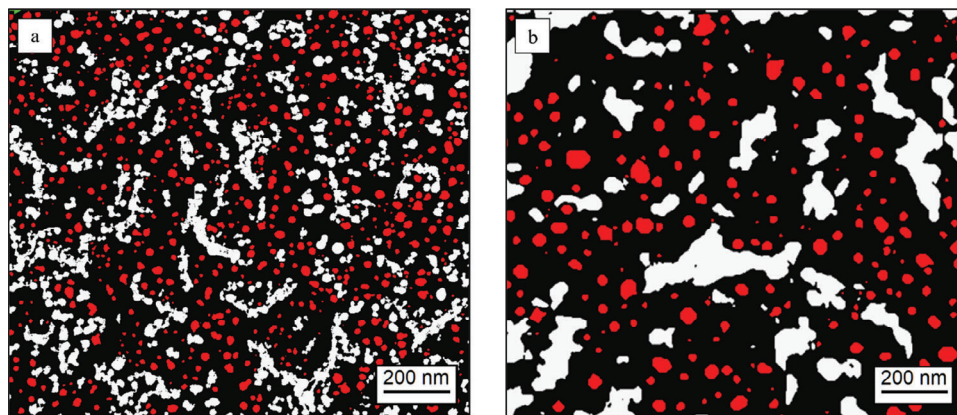
Strategies such as optimizing sputtering parameters, membrane preconditioning, and nanoparticle capping can contribute to improved coating durability. The scalability of the sputtering process for large-scale membrane production is a key challenge that requires further investigation and optimization. While this study demonstrates the potential of MNP coatings for enhancing membrane antimicrobial properties, further research is necessary to address the long-term stability of these coatings, their potential environmental and health implications in water treatment applications, and the development of scalable manufacturing processes.

4. Experimental Section

Materials: TFC aromatic PA membranes (AG H elements) were obtained from SUEZ WTS Germany GmbH. Following the manufacturer's recommendations, the membranes were stored at 4 °C in a 1 wt.-% sodium bisulfite solution until use.

Prior to coating deposition, the membranes were rinsed in PBS and then dried at room temperature for 24 h. PBS was prepared according to Dulbecco and Vogt,[59] using 137 mM sodium chloride (AnalaR NORMAPUR, VWR, 99.9%), 1.5 mM potassium dihydrogen phosphate (Carl Roth, > 98%), 8.1 mM disodium hydrogen phosphate (Carl Roth, ≥ 99%) and 2.7 mM potassium chloride (Carl Roth, > 99.5%). This rinsing step was essential to maintain the membrane performance during the drying process.[33]

Plasma-Enhanced Magnetron Sputtering: Silver, copper, and gold nanoparticles were deposited from spherical sputter targets (Ag: Target Materials, Inc., 99.9%; Au: ESG Edelmetall-Service GmbH & Co. KG, 99.99%; Cu: made in-house, 99.9%) using radio frequency (r.f.) magnetron sputtering (VEB Hochvakuum Dresden) at 13.56 MHz. The coating deposition was conducted at a power of 200 W, a partial pressure of 1 x 10^{-2} mbar ± 2 x 10^{-4} mbar and an argon gas flow rate of 33 sccm.

**ADVANCED
SCIENCE NEWS**

www.advancedsciencenews.com

**ADVANCED
MATERIALS
INTERFACES**
Open Access

www.advmatinterfaces.de

Figure 8. Particle size analysis on a silver-coated RO composite membrane (coating parameters: P = 200 W, t = 3 x 5 s). For quantification, only discrete particles (red) were considered; coherent clusters (white) were not included. a) Particle size distribution after coating (reference), b) Particle size distribution after elution (24 h, 2 g L^{-1} NaCl solution).

Total deposition times varied from 1 to 50 s to produce nanoparticle distributions with varying density and coverage. To prevent material degradation due to heat exposure, sputtering was performed in 5 s increments.

XPS: XPS was used to analyze the surface composition of the TFC membranes after each modification step. The measurements were carried out using a Kratos AXIS Ultra^{DLD} (Kratos Analytical Ltd.) device at a pressure of 1×10^{-8} mbar to 1×10^{-9} mbar. For each sample, three measurement points were analyzed, each with an area of 700×300 μm^2. The detection depth was estimated to be 5 to 10 nm. Survey spectra were recorded with a pass energy of 160 eV and a step width of 0.1 eV.

Data processing and peak assignment were performed using CasaXPS (Version 2.3.15, Casa Software Ltd.). The binding energy scale was calibrated with respect to the C 1s peak at 284.5 eV. For quantitative evaluation of the spectra, the relative sensitivity factors (R.S.F.) provided by the instrument manufacturer were used.

SEM: The surface morphology of native and MNP-coated RO membranes was examined using SEM with a Quanta 3D FEG (Thermo Fisher Scientific/FEI) device. All samples were mounted on standard SEM sample holders. To prevent surface charging, a thin platinum layer was applied to all samples except those used for imaging the metal nanoparticles. Image acquisition was performed in secondary electron (SE) mode at an accelerating voltage of 10 kV. The diameter of the metal nanoparticles and the degree of coverage were determined using image processing software (cell^F, Olympus Soft Imaging Solutions GmbH).

EDS mappings were conducted on selected samples to analyze the distribution and concentration of the MNPs. Each case examined a sample area of 16×16 μm^2. Semiquantitative elemental analysis was performed using an Xplore 15 detector in combination with AZtecLiveLite software.

Contact Angle Measurements: Contact angle measurements were performed to evaluate the surface wettability of native and MNP-coated membranes using a static sessile drop method in air (Krüss Advance 1.13.1.31401). Diiodomethane and double-distilled water (ddH$_2$O) served as the liquid phases. Surface energy, along with its polar and dispersive components, was calculated using the Owens, Wendt, Rabel, and Kaelble (OWRK) method. A minimum of 10 valid measurements were taken for each sample.

Biofouling Tests and Fluorescence Microscopy: The antimicrobial activity of MNP coatings was investigated through static bacterial suspension tests using *P. protegens* (CHA0; DSM-19095). This strain was selected because *Pseudomonas* species are commonly found in biofilms on RO membranes.[60,61] The bacterial strains were stored at −80 °C following the supplier's recommendations. Bacterial cell cultures were prepared by adding 10 μL of bacterial stock solution to 50 mL of tryptone soy broth (Carl Roth). Both a preculture and a main culture were prepared for each run. The bacterial cells were incubated at 25 °C and 120 rpm shaking speed

(Unimax 2010, Heidolph). After an incubation period of 18 to 24 h, the bacterial cells were thoroughly rinsed and resuspended in ddH$_2$O.

Native and MNP-coated membranes were sterilized with 70% isopropanol and placed in a 12-well plate. 1 mL of an aqueous bacterial suspension with an optical density of 0.1 (OD600 DiluPhotometer, IMPLEN) was added to each well. After 2 h, the membranes were withdrawn and transferred to a fresh nutrient medium for 18 h. The number of CFUs in the supernatant solution of the coated membranes was determined as a measure of bacterial growth. A dilution series was prepared from the supernatant, and 50 μl of each dilution was spread on agar plates (Plate-Count-Agar, Carl Roth). After an incubation period of 48 h at 37 °C, the CFU was counted, and the logarithmic reduction factor $Log_{10}(CFU_0/CFU)$ was calculated relative to the control group (uncoated membrane). The statistical significance of the measurement results was evaluated using a non-parametric Mann-Whitney U test (α = 0.05; OriginPro2021b, Origin-Lab Corporation).

Bacterial growth on the membrane surface was examined by fluorescence microscopy and SEM. For fluorescence microscopy, the intact biofilms were rinsed with ddH$_2$O and sequentially stained with SYTO 9 (Fisher Scientific) and propidium iodide ($\geq$ 94%, Acros Organics). Image acquisition was performed with a Keyence BZ-X800E fluorescence microscope in z-stack mode, employing Fluor GFP and Fluor TxRed filters to visualize viable and non-viable bacteria, respectively.

For SEM investigation, the membranes were immersed in a PBS solution containing 2.5% glutaraldehyde (Carl Roth) overnight. After several rinsing steps, the samples were exposed to liquid nitrogen and freeze-dried for 18 h (Alpha 2–4 LSCplus; Christ). Sample preparation for SEM followed previously described procedures.

Filtration Performance Tests: The filtration performance of native and MNP-coated RO membranes was measured using an in-house developed coupon test system. This system comprises six measurement cells arranged in a linear configuration. Round-cut membrane coupons with a diameter of 7.5 cm were inserted, and feed water was forced through the cells at a defined pressure (15.6 bar $\pm$ 1 bar) and temperature (24 °C $\pm$ 0.5 °C). Temperature stability was maintained by a recirculating chiller. The feed water conductivity was set to 3500 μS m^{-1}, corresponding to an aqueous solution containing 2 g L^{-1} NaCl. The pH value of the feed water was continuously adjusted to 7.0 $\pm$ 0.2 by means of an automatic control unit.

Permeate was collected at regular time intervals, and the mass (m_1) and conductivity (σ_1) of the samples were determined. The flow rate (J) was calculated as a function of the cross-sectional area (A) of the membrane and the collecting time (t) using Equation (1). The salt retention (R_S), related to the sodium chloride concentration in the permeate (c_1) and in the feed solution (c_{Feed}), was determined according to Equation (2). Given that there is no linear relationship between concentration and electrical

2400461 (8 of 10)

conductivity in the concentration range considered, the sodium chloride concentration was calculated using Equation (3).[62]

$$J = \frac{m_1}{\rho_1 \cdot A \cdot t} \tag{1}$$

$$R_S = \left(1 - \frac{c_1}{c_{Feed}} \right) \tag{2}$$

$$c_1 = 0,4264 \cdot \sigma_1^{1,0457} \tag{3}$$

Coating Stability Tests: MNP-coated, round-cut membranes with a diameter of 1.27 cm (1″) were placed in 10 mL of an aqueous sodium chloride solution (2 g L^{-1}) at a shaking speed of 80 rpm. After 24 h, the membranes were withdrawn and prepared for analysis by XPS and SEM.

The metal content in the eluate was determined using ICP-MS (ELEMENT XR, Thermo Scientific). To achieve a homogeneous sample solution and ensure complete dissolution of the MNPs, chemical digestion in an acid solution was performed. First, the primary solvent was evaporated at 125 °C. Subsequently, 3 mL of acid solution (3:1 (v/v) of HCl (37%): HNO$_3$ (65%) for samples containing gold or 2:1 (v/v) of HNO$_3$ (65%): ddH$_2$O for samples containing silver and copper) was added to each residue. The samples were heated to the boiling point for 10 min and then diluted with 10 mL of ddH$_2$O. All elements were measured in medium resolution using a combined secondary electron multiplier and Faraday detector, which has a dynamic detection range of 0.2 cps to $> 10^{12}$ cps.

Statistical Analysis: Measured values are presented as mean ± standard deviation. Data pre-processing, including normalization, and sample sizes are specified in the relevant sub-sections. To assess statistical significance, the normality of data distribution was tested using the Shapiro-Wilk test ($\alpha = 0.05$), and the homogeneity of variances was evaluated using Levene's test ($\alpha = 0.05$). When data met the criteria for normality and homogeneity, either an independent samples t-test or a paired samples t-test was employed. If these criteria were not met, non-parametric tests such as the Mann-Whitney U test were used. Statistical analysis was performed using OriginPro2021b (OriginLab Corporation).

Supporting Information

Supporting Information is available from the Wiley Online Library or from the author.

Conflict of Interest

The authors declare no conflict of interest.

Data Availability Statement

The data that support the findings of this study are available from the corresponding author upon reasonable request.

[1] S. Ahuja, in *Advances in Water Purification Techniques*, (Ed: S. Ahuja), Elsevier, Cambridge, Massachusetts, United States **2019**, Ch2.
[2] E. Jones, M. Qadir, M. T. Van Vliet, V. Smakhtin, S.-M. Kang, *Sci. Total Environ.* **2019**, *657*, 1343.
[3] A. Karabelas, C. Koutsou, M. Kostoglou, D. Sioutopoulos, *Desalination.* **2018**, *431*, 15.
[4] K. Harby, E. S. Ali, K. Almohammadi, *J. Cleaner Prod.* **2021**, *287*, 125014.
[5] J. Kim, K. Park, S. Hong, *J. Membr. Sci.* **2020**, *601*, 117889.
[6] J. Choi, Y. Oh, S. Chae, S. Hong, *Desalination.* **2019**, *462*, 19.
[7] I. Nurjanah, T.-T. Chang, S.-J. You, C.-Y. Huang, W.-Y. Sean, *Desalination.* **2024**, *581*, 117590.
[8] S. S. Cob, F. G. Güner, B. Hofs, J. Van Spronsen, G.-J. Witkamp, *Desalination.* **2014**, *344*, 36.
[9] M. Qasim, M. Badrelzaman, N. N. Darwish, N. A. Darwish, N. Hilal, *Desalination.* **2019**, *459*, 59.
[10] S. Jiang, Y. Li, B. P. Ladewig, *Sci. Total Environ.* **2017**, *595*, 567.
[11] F. Seyedpour, J. Farahbakhsh, Z. Dabaghian, W. Suwaileh, M. Zargar, A. Rahimpour, M. Sadrzadeh, M. Ulbricht, Y. Mansourpanah, *Desalination.* **2024**, *581*, 117614.
[12] M. Ginic-Markovic, T. G. Barclay, K. T. Constantopoulos, E. Markovic, S. R. Clarke, J. G. Matisons, *Desalination.* **2015**, *369*, 37.
[13] J. Wu, Z. Wang, W. Yan, Y. Wang, J. Wang, S. Wang, *J. Membr. Sci.* **2015**, *496*, 58.
[14] S. Laghmari, P. May, M. Ulbricht, *J. Membr. Sci.* **2021**, *629*, 119274.
[15] Y.-G. Wu, M.-Y. Jiang, J. Zhao, Y.-J. Cai, X.-Z. Li, X. Yang, H. Jiang, Y.-X. Sun, N.-J. Wei, Y. Liu, *Colloids Surf., A.* **2023**, *679*, 132642.
[16] M. R. Hibbs, L. K. Mcgrath, S. Kang, A. Adout, S. J. Altman, M. Elimelech, C. J. Cornelius, *Desalination.* **2016**, *380*, 52.
[17] F. Perreault, M. E. Tousley, M. Elimelech, *Environ. Sci. Technol. Lett.* **2014**, *1*, 71.
[18] I. Abdulazeez, A. Matin, M. Khan, M. Khaled, M. Ansari, S. Akhtar, S. Rehman, *J. Membr. Sci.* **2019**, *591*, 117299.
[19] E. Sánchez-López, D. Gomes, G. Esteruelas, L. Bonilla, A. L. Lopez-Machado, R. Galindo, A. Cano, M. Espina, M. Ettcheto, A. Camins, *Nanomaterials.* **2020**, *10*, 292.
[20] E. Bressan, L. Ferroni, C. Gardin, C. Rigo, M. Stocchero, V. Vindigni, W. Cairns, B. Zavan, *Int J Dent.* **2013**, *2013*, 8.
[21] H. Lee, D. G. Lee, *Colloids Surf., B.* **2018**, *167*, https://doi.org/10.1016/j.colsurfb.2018.03.049.
[22] G. Wang, H. Hou, S. Wang, C. Yan, Y. Liu, *Colloids Surf., B.* **2017**, *157*, 138.
[23] M. Ben-Sasson, X. Lu, E. Bar-Zeev, K. R. Zodrow, S. Nejati, G. Qi, E. P. Giannelis, M. Elimelech, *Water Res.* **2014**, *62*, 260.
[24] D. Suresh, P. S. Goh, T. W. Wong, L. Zhang, A. F. Ismail, *Desalination.* **2024**, *569*, 117040.
[25] J. Yin, Y. Yang, Z. Hu, B. Deng, *J. Membr. Sci.* **2013**, *441*, 73.
[26] C. Dong, Z. Wang, J. Wu, Y. Wang, J. Wang, S. Wang, *Desalination.* **2017**, *401*, 32.
[27] P. G. Torres-Valenzuela, J. Álvarez-Sánchez, G. E. Dévora-Isiordia, M. M. Armendáriz-Ontiveros, M. Del Rosario Martínez-Macias, S. Pérez-Sicairos, R. G. Sánchez-Duarte, G. A. Fimbres Weihs, *Polym. Bull.* **2023**, *80*, 6285.
[28] S.-H. Park, S. H. Kim, S.-J. Park, S. Ryoo, K. Woo, J. S. Lee, T.-S. Kim, H.-D. Park, H. Park, Y.-I. Park, *J. Membr. Sci.* **2016**, *513*, 226.
[29] U. M. Hirsch, N. Teuscher, M. Rühl, A. Heilmann, *Surf. Interfaces.* **2019**, *16*, https://doi.org/10.1016/j.surfin.2019.04.003.
[30] K. Zheng, M. I. Setyawati, D. T. Leong, J. Xie, *Coord. Chem. Rev.* **2018**, *357*, 1.
[31] M. L. Ermini, V. Voliani, *ACS Nano.* **2021**, *15*, 6008.
[32] X. Gu, Z. Xu, L. Gu, H. Xu, F. Han, B. Chen, X. Pan, *Environ. Chem. Lett.* **2021**, *19*, 167.
[33] N. Michler, Dissertation, Martin-Luther-Universität, Halle-Wittenberg **2023**.

**ADVANCED
SCIENCE NEWS**

www.advancedsciencenews.com

**ADVANCED
MATERIALS
INTERFACES**
Open Access

www.advmatinterfaces.de

[34] Y. Jin, S. Liang, Z. Wu, Z. Cai, N. Zhao, *Appl. Surf. Sci.* **2014**, *314*, 286.

[35] A. Heilmann, *Polymer Films with Embedded Metal Nanoparticles*, Springer, Berlin, Germany **2003**.

[36] M. Mcmahon, R. Lopez, H. Meyer, L. Feldman, R. Haglund, *Appl. Phys. B: Lasers Opt.* **2005**, *80*, 915.

[37] S. D. Ekpe, L. W. Bezuidenhout, S. K. Dew, *Thin Solid Films.* **2005**, *474*, 330.

[38] A. Ueda, H. Saneoka, *Curr. Microbiol.* **2015**, *70*, 506.

[39] L. D. Villa-García, R. Márquez-Preciado, M. Ortiz-Magdaleno, O. A. Patrón-Soberano, M. A. Álvarez-Pérez, A. Pozos-Guillén, L. O. Sánchez-Vargas, *Braz J Microbiol.* **2021**, *52*, 619.

[40] Y. Zhang, T. P. Shareena Dasari, H. Deng, H. Yu, *J. Environ. Sci. Health, Part C: Environ. Carcinog. Rev.* **2015**, *33*, 286.

[41] G. Burygin, B. Khlebtsov, A. Shantrokha, L. Dykman, V. Bogatyrev, N. Khlebtsov, *Nanoscale Res. Lett.* **2009**, *4*, 794.

[42] A. Wernicki, A. Puchalski, R. Urban-Chmiel, M. Dec, D. Stegierska, A. Dudzic, A. Wojcik, *Med Weter.* **2014**, *70*, 564.

[43] K. Gold, B. Slay, M. Knackstedt, A. K. Gaharwar, *Adv. Ther.* **2018**, *1*, 1700033.

[44] K. Zheng, M. I. Setyawati, D. T. Leong, J. Xie, *ACS Nano.* **2017**, *11*, 6904.

[45] C. Y. Tay, Y. Yu, M. I. Setyawati, J. Xie, D. T. Leong, *Nano Res.* **2014**, *7*, 805.

[46] R. Büssing, B. Karge, P. Lippmann, P. G. Jones, M. Brönstrup, I. Ott, *ChemMedChem.* **2021**, *16*, 3402.

[47] Y. Zong, R. Zhang, S. Gao, H. Chang, B. Van Der Bruggen, J. Tian, *J. Membr. Sci.* **2021**, *638*, 119721.

[48] R. Dehghan, J. Barzin, *J. Polym. Res.* **2021**, *28*, 76.

[49] M. Nilsson, G. Trägårdh, K. Östergren, *J. Membr. Sci.* **2006**, *280*, 928.

[50] S. Xiao, B. Ren, L. Huang, M. Shen, Y. Zhang, M. Zhong, J. Yang, J. Zheng, *Curr. Opin. Chem. Eng.* **2018**, *19*, 86.

[51] B. Wang, Y. Zhang, W. Liang, G. Wang, Z. Guo, W. Liu, *J. Mater. Chem. A.* **2014**, *2*, 7845.

[52] M. R. Shirazy, S. Blais, L. G. Fréchette, *Appl. Surf. Sci.* **2012**, *258*, 6416.

[53] N. Sabri, H. Hasbullah, N. Said, N. Ibrahim, R. Kasmani, R. Ali, S. Rahman, *J. Appl. Membr. Sci. & Technol.* **2017**, *20*, 1.

[54] Y. Haoyong, J. Zhensheng, Z. Shunli, W. Shoubin, Z. Zhijun, *Sci. China, Ser. B: Chem.* **2002**, *45*, 625.

[55] X. Qian, X. Pang, K. Gao, H. Yang, J. Jin, A. A. Volinsky, *J. Mater. Eng. Perform.* **2014**, *23*, 786.

[56] K. Loza, J. Diendorf, C. Sengstock, L. Ruiz-Gonzalez, J. Gonzalez-Calbet, M. Vallet-Regi, M. Köller, M. Epple, *J. Mater. Chem. B.* **2014**, *2*, 1634.

[57] A. Dey, A. Dasgupta, V. Kumar, A. Tyagi, A. K. Verma, *Int Nano Lett.* **2015**, *5*, 223.

[58] T. Jayaramudu, K. Varaprasad, R. D. Pyarasani, K. K. Reddy, K. D. Kumar, A. Akbari-Fakhrabadi, R. Mangalaraja, J. Amalraj, *Int. J. Biol. Macromol.* **2019**, *128*, 499.

[59] R. Dulbecco, M. Vogt, *J. Exp. Med.* **1954**, *99*, 167.

[60] J. Baker, L. Dudley, *Desalination.* **1998**, *118*, 81.

[61] O. Sánchez, *J. Membr. Sci.* **2018**, *545*, 240.

[62] U. Hirsch, Dissertation, Martin-Luther-Universität, Halle-Wittenberg **2015**.